理學碩士 學位 論文

Dual Synergies of Hollow CdS Cubes on MoS_2 sheets for Enhanced Visible-Light-Driven photocatalysis

(가시광을 활용하는 광촉매의 향상된 활성을 위한 속 빈 황화카드뮴 큐브와 이황화몰리브덴 시트의 이중 시너지 효과)

蔚 山 大 學 校 大 學 院

化 學 科

徐 昨 伶

Dual Synergies of Hollow CdS Cubes on MoS_2 sheets for Enhanced Visible-Light-Driven photocatalysis

指 導 敎 授 홍 종 욱

이 論文을 理學碩士 學位 論文으로 제출함

2024年 02月

蔚 山 大 學 校 大 學 院

化 學 科

徐 昕 伶

徐 昨 伶의 理學碩士 學位 論文을 認准함

審査委員 이 민 형 印

審査委員 홍 종 욱 印

審査委員 김 범 진 印

蔚 山 大 學 校 大 學 院

2024年 02月

국문요약

현재 주요 에너지원으로 사용되고 있는 화석연료는 한정적인 매장량과 연소 시 발생하는 온실가스로 인한 환경오염 발생이라는 문제가 있다. 이를 해결하기 위해 화석연료를 대체할 신재생 에너지로 수소 에너지가 주목받고 있다. 수소 에너지의 원료가 되는 수소의 96%는 현재 화석연료로부터 생산되어 이산화탄소를 만들어내는 그레이 수소이다. 광촉매는 태양에너지를 화학 에너지로 변환하여 물을 분해해 수소를 생성할 수 있으며 별도의 온실 가스 배출이 없다는 점에서 주목받고 있다. 일반적으로 반도체를 광촉매로 사용하지만 단일 반도체의 경우 표면적이 작고 흡수할 수 있는 빛의 범위가 제한적이며 내구성이 낮기 때문에 두가지 이상의 반도체를 결합하여 위의 한계를 극복하고자 하는 연구가 진행되고 있다.

촉매의 활성을 높이는 방법에는 모양을 조절하여 표면적을 증가시키는 방법과 활성이 좋은 입자를 내구성과 전하이동성이 우수한 지지체 위에 올리는 방법이 있다. 2.38 eV의 밴드갭을 가지는 CdS는 가시광선부터 근적외선에 해당하는 넓은 범위의 빛을 흡수하여 활성화되기 때문에 각광받는 한편, 낮은 공간 전하 분리, 느린 전하 이동 속도, 낮은 내구성의 한계로 단일 광촉매로 사용할 경우 낮은 광촉매 활성은 보인다. MoS_2 시트는 넓은 표면적을 가지며 내구성이 뛰어나고 수소 생선 반응에 적합한 활성 사이트를 가지고 있다. 속이 빈 나노 구조가 가지는 투과성은 활성 사이트에서 다중 광 산란을 통해 광 활용도를 향상시키며 표면적을 넓히기 때문에 광촉매 활성을 높일 수 있다.

이 연구에서는 Cu_2O 나노 큐브 입자를 MoS_2 시트 위에 성장시켜 Cu_2O/MoS_2 이종접합 헤테로 나노 구조체를 합성한 뒤 양이온 교환 방법을 통해 속 빈 Cu_2S/MoS_2 헤테로 나노 구조체(H-Cu_2S/MoS_2 HNSs)와 속 빈 CdS/MoS_2 헤테로 나노 구조체(H-CdS/MoS_2 HNSs)를 합성하였으며 대조군으로 단일 Cu_2O, H-Cu_2S, 그리고 H-CdS 나노 큐브 입자를 선택하여 광촉매 활성을 비교하였다. 주사 전자 현미경과 투과 전자 현미경을 통해 속 빈 CdS 큐브 나노 입자와 MoS_2 시트의 결합을 확인하였으며 X선 회절 분석법과 X선 광전자 분석법을 통해 각 광촉매의 결정구조와 표면 전자 거동의 변화를 확인하였다. 확산 반사 분광법과 Mott-

Schottky 분석을 통해 수소 생성 반응 메커니즘을 알아보았다.

합성한 촉매의 활성을 비교하기 위해 수소 생성 반응을 가시광선 하에서 진행하였으며 H-CdS/MoS_2 HNSs가 단일 H-CdS 큐브 나노 입자보다 10배 이상 높은 활성을 나타내었다. 뿐만 아니라 유기 오염물의 분해에서도 H-CdS/MoS_2 HNSs는 동일 시간 내에 가장 많은 오염물을 분해하며 높은 활성을 보였으며 전기화학 임피던스 분광법에서 가장 낮은 저항을 보였다. 이는 CdS 큐브 나노 입자와 MoS_2 시트 사이의 접합으로 인해 전하 분리 및 전달 기능이 향상되었으며 속이 빈 CdS 나노 입자 내부의 다중 산란으로 인해 표면적 증가 및 광흡수 효율이 증가하여 촉매 활성이 증가한 것임을 알 수 있다.

Abstract

Fossil fuels, which are currently used as the main source of energy, have limited reserves and cause environmental pollution due to greenhouse gases generated during combustion. To solve this problem, hydrogen energy is gaining attention as a renewable energy to replace fossil fuels. Currently, 96% of the hydrogen used for hydrogen energy is gray hydrogen, which is produced from fossil fuels and produces carbon dioxide. Photocatalysts are attracting attention because they can convert solar energy into chemical energy to decompose water to produce hydrogen, and there are no greenhouse gas emissions. In general, semiconductors are used as photocatalysts, but since a single semiconductor has a small surface area, a limited range of light absorption, and low durability, researchers are trying to overcome the above limitations by combining two or more semiconductors.

There are two ways to increase the activity of the catalyst: by adjusting the morphology to increase the surface area, and by placing the active particles on a durable and electrolytic support. CdS, with a bandgap of 2.38 eV, has gained attention because it is activated by absorbing a wide range of light from visible to near-infrared, but its low spatial charge separation, slow charge transfer rate, and low durability limit its photocatalytic activity when used as a single photocatalyst. MoS_2 sheets have a large surface area, are durable, and have active sites suitable for the hydrogen evolution reaction. The permeability of hollow nanostructures can enhance light utilization through multiple light scattering from the active sites and increase the surface area, thereby increasing the photocatalytic activity.

In this study, Cu_2O cube particles were grown on MoS_2 sheets to synthesize Cu_2O/MoS_2 hetero-nanostructures, and then hollow Cu_2S/MoS_2 hetero-nanostructures (H-Cu_2S/MoS_2 HNSs) and hollow CdS/MoS_2 hetero-nanostructures (H-CdS/MoS_2 HNSs) were synthesized by anion and cation exchange method, and single Cu_2O, H-Cu_2S, and H-CdS cube were selected counterparts to compare their photocatalytic activities. Scanning electron microscopy and transmission electron microscopy confirmed the intimate interfaces of hollow CdS cube nanoparticles with MoS_2 sheets, while X-ray diffraction and X-ray photoelectron spectroscopy confirmed the changes in the crystal structure and surface electronic behavior of each photocatalyst. Diffuse reflectance spectroscopy and Mott-Schottky analysis were used to investigate the hydrogen evolution reaction mechanism.

To compare the activity of the synthesized catalysts, the hydrogen evolution reaction was carried out under UV-visible light, and the H-CdS/MoS_2 HNSs showed more than 10 times higher activity than H-CdS cubes. In addition, in the degradation of organic pollutants, the H-CdS/MoS_2 HNSs showed the highest activity, degrading the most pollutants at the same time, and the lowest resistance in electrochemical impedance spectroscopy. This indicates that the conjugation between CdS cube nanoparticles and MoS_2 sheets enhanced the charge separation and transfer function, and the multiple scattering inside the hollow CdS nanoparticles increased the surface area and increased the light absorption efficiency, resulting in the increased catalytic activity.

Index

I. Introduction

Harnessing renewable and clean energy from sunlight offers an effective solution to tackle the worldwide energy crisis and environmental concerns[1-5]. Photocatalytic hydrogen generation, which converts solar energy into chemical energy, has emerged as one of the most promising strategies for sustainable energy conversion[6-10]. Semiconductor nanomaterials, notably transition metal sulfides such as extensively investigated CdS, have gained prominence as intriguing catalysts active in the visible-to-near-infrared light range for the photocatalytic hydrogen production through water splitting[11-13]. This is attributed to their unique physical, chemical, and catalytic properties [14, 15]. However, the relatively limited durability, low spatial charge separation, and slow carrier migration kinetics of individual CdS often impede energy conversion efficiencies and the practical application of photocatalytic hydrogen production. In contrast, heteronanostructures (HNSs) that combine two or more distinct semiconductor components within a single system, resulting in effective functionalities induced by well-defined and intimate interfaces, have attracted significant attention due to their captivating properties and diverse potential applications[16, 17]. Chemically exfoliated MoS_2 sheets, a representative layered transition metal sulfide, stand as promising candidates for the preparation of effective HNSs for photocatalytic hydrogen production when integrated with CdS materials[18, 19]. This can be attributed their high charge carrier mobility, adjustable band gap for visible light absorption, substantial surface area, and strong chemical stability[20, 21]. Furthermore, MoS_2 sheets have demonstrated potential as catalysts for the hydrogen evolution reaction (HER) due to the presence of active edge sites conducive to this reaction. Therefore, HNSs including MoS_2 have recently shown promise as cost-effective cocatalysts for water activation in hydrogen production, exhibiting comparable activity to that of noble metals such as Pt, Pd, and Ru[22, 23].

In addition to the formation of HNSs, the precise control of semiconductor morphology represents a promising strategy for the synthesis of advanced photocatalysts tailored for efficient photocatalytic hydrogen production[24-26]. Among various morphologies, hollow-structured semiconductors have attracted significant attention in recent years due to their distinctive physical and chemical properties, as well as their potential applications in photocatalysis[27-29]. Notably, the substantial surface area and excellent permeability of hollow nanostructures facilitate increased active sites and enhanced light utilization through multiple light scattering, rendering them ideal candidates for highly efficient photocatalysis. Consequently, there is a

compelling interest in the development of photocatalysts based on hollow CdS nanostructure/MoS_2 materials. However, the intricate fabrication processes associated with hollow CdS nanostructure/MoS_2 materials pose challenges in achieving both highly monodisperse size and morphology, thereby limiting their practical utility as effective photocatalysts.

Herein, we present a novel synthetic strategy for hollow CdS cube/MoS_2 sheet HNSs (H-CdS/MoS_2 HNSs) by leveraging anion and cation exchange processes. The schematic illustration of the synthesis procedure for the H-CdS/MoS_2 HNSs is provided in Figure 1a. This synthesis method facilitates the formation of intimate interfaces between hollow CdS cubes (H-CdS cubes) and MoS_2 sheets. The resulting intimate interfaces between H-CdS cubes and MoS_2 sheets promotes efficient charge separation and migration, crucial for enhancing photocatalytic hydrogen production. Furthermore, the hollow morphology of the CdS domain enhances both light-harvesting efficiency through multi-light scattering, while the MoS_2 sheets contribute large active sites for HER owing to their thin 2D morphology. For photocatalytic HER under visible light irradiation, H-CdS/MoS_2 HNSs demonstrated significantly higher photocatalytic activity compared to hollow Cu_2S cube/MoS_2 sheet (H-Cu_2S/MoS_2 HNSs), Cu_2O cube/MoS_2 sheet (Cu_2O/MoS_2 HNSs), and their unary counterparts (H-CdS, H-Cu_2S, and Cu_2O cubes), which can be attributed to the synergistic advantages arising from their effective composition and structural features. We believe that this novel strategy holds promising potential for the development of high-efficiency and cost-effective photocatalysts with precisely controlled morphologies and structures.

II. Experimental

Chemicals and materials. Molybdenum(IV) sulfide (MoS_2), n-butyllithium solution (2.5 M in hexanes), copper(II) chloride ($CuCl_2$, 99.999%), sodium dodecyl sulfate (SDS, ≥99.0%), hydroxylamine hydrochloride ($NH_2OH{\cdot}HCl$, 98.0%), hydrazine monohydrate (N_2H_4, 64-65%), sodium sulfide nonahydrate ($Na_2S{\cdot}9H_2O$, ≥ 99.99%), Tri-n-butylphosphine (TBP, 99%), methyl orange (85% dyes), and Ciprofloxacin hydrochloride were provided by Sigma Aldrich. Cadmium nitrate tetrahydrate ($Cd(NO_3)_2{\cdot}4H_2O$, 99.9%, Alfa Aesar), hydrochloric acid (35.0-37.0%, DAEJUNG), citric acid (CA, 99%, pure, anhydrous, Acros Organics), methanol (CH_3OH, 99.999%, SK chemicals), sodium hydroxide beads (NaOH, 97%, DAEJUNG). Ultrapure distilled and deionized water (18.2 MΩ) was used for all solution preparations.

Preparation of MoS_2 sheets. According to the previous report[30], preparation of MoS_2 sheets was carried out through chemical exfoliation. 0.5 g of bulk-MoS_2 was added to 5 mL of n-butyllithium (2.5 M in hexanes) under Ar atmosphere. The mixture was maintained at room temperature for 2 days. After sonication for 30 min, MoS_2 sheets were collected from the bulk MoS_2 by centrifugation (5000 rpm for 10 min and 10,000 rpm for 10 min).

Synthesis of Cu_2O/MoS_2 HNSs. To prepare Cu_2O/MoS_2 HNSs, a mixture composed of 11.84 mL of deionized water, 2 mL of MoS_2 sheet solution (0.5 mg), and 2 mL of 0.095 mM CA was stirred at 40 °C in a water bath for 1 hour. Subsequently, a solution containing 3.6 mL of 100 mM SDS and 0.4 mL of 100 mM $CuCl_2$ was introduced into the reaction mixture, Finally, 0.144 mL of 1.0 M NaOH and 0.4 mL of 100 mM $NH_2OH{\cdot}HCl$ were added sequentially, the mixture was held for 1 h at 33 °C. The reaction mixture was purified by centrifugation at 5000 rpm for 10 min. The precipitate was washed using methanol (5 mL), then subjected to centrifugation at 5000 rpm for 5 min. The final product was redispersed in 5 mL of methanol.

Synthesis of H-Cu_2S/MoS_2 HNSs. The as synthesized Cu_2O-MoS_2 solution in methanol (5 mL) were cooled in an ice-bath for 5 min. $Na_2S_{(aq)}$ (0.4 mL, 0.05 M, 5.0 μmol) was added to the suspension, then stirred for 30 s to convert the surfaces of the Cu_2O into Cu_2S cubes. The suspension was centrifuged at 5000 rpm for 5 min, then the precipitate was dispersed in methanol (5 mL). To create the hollow structure, 0.4 mL of 2.0 M HCl was added with shaking for 30 s. The solution turned brown immediately, indicating the formation of hollow

Cu_2S cubes. The suspension was centrifuged at 5000 rpm for 10 min, then redispersed in methanol (5 mL) for the subsequent cation exchange reaction from Cu_2S to CdS.

Synthesis of H-CdS/MoS_2 HNSs. A mixture of $Cd(NO_3)_2 \cdot 4H_2O$ in methanol (2.5 mL, 0.2 M, 0.5 mmol) and TBP in toluene (2.5 mL, 0.4 M, 1.0 mmol) was added dropwise to the mixture of H-Cu_2S/MoS_2 HNSs (5 mL) in methanol at ambient temperature under sonication. As the exchange reaction proceeded for 30 minutes, the brown solution gradually turning green. The resulting mixture was then cleaned through centrifugation at 6500 rpm for 10 min twice. We synthesized pristine Cu_2O, H-Cu_2S, and H-CdS cubes using the same process, except for the exclusion of MoS_2 sheets.

Characterization. Scanning electron microscopy (SEM) and transmission electron microscopy (TEM) images of the synthesized nanostructures were obtained using Jeol JEM-7210F and Jeol JEM-2100F, respectively. Inductively coupled plasma-optical emission spectrometry (ICP-OES) measurements were conducted using a Spectroublue-ICP-OES (Ametek). X-ray diffraction (XRD) measurements were conducted on a Rigaku D/MAX2500V/PC. The Raman spectra were obtained through confocal Raman spectroscopy using a 532-nm laser and a 1200 grating (NOST, HEDA). X-ray photoelectron spectroscopy (XPS) measurements were conducted using a Thermo VG Scientific Sigma Probe spectrometer with Al Kα X-ray (1486.6 eV) as a light source. XPS data were calibrated using the C 1s peak at 284.5 eV. The UV-vis spectra and the photocatalytic activity of the photocatalysts for ciprofloxacin degradation were measured by a Shimadzu UV-2600 spectrometer. Electrochemical impedance spectroscopy (EIS) was performed using an EC-Lab Biologic Model SP-300 potentiostat. The amount of H_2 evolved was measured by gas chromatography (GC, Agilent 7890 B). SEM and GC analyses were conducted using instruments at the Total-Period Analysis Center for the Ulsan Chemical Industry of the Korea Basic Science Institute (KBSI).

Photocatalysis Experiments. Photocatalytic hydrogen evolution and ciprofloxacin degradation experiments were carried out under visible-light irradiation using a Xe lamp (300 W, Newport 66902) equipped with a UV-cut filter that transmits light in the range of $\lambda > 420$ nm. The intensity of light in the cell was measured to be 100 mW cm^{-2}. In typical photocatalytic hydrogen evolution experiments, 2.5 mg of photocatalysts was added in 20 mL of methanol:deionized water (1:3) mixture. In typical degradation of ciprofloxacin and methyl orange experiments, 2.5 mg of photocatalysts was added in 20 mL of an aqueous

mixture including 0.078 mM of ciprofloxacin hydrochloride and 0.092 mM of methyl orange. For photocatalytic hydrogen evolution, the mixture was purged with Ar for 40 min. The amount of hydrogen produced by photocatalysts was obtained by GC and the photocatalytic ciprofloxacin and methyl orange degradation activities were measured by a Shimadzu UV-2600 spectrometer.

Electrochemical experiments. Electrochemical experiments were performed in a three-electrode cell using EC-Lab Biologic Model SP-300 potentiostats. Graphite rods and Hg/HgO (3.0 mol/L NaOH) were used as the counter and reference electrodes, respectively. The working electrode was prepared by dropping 5 μL of the photocatalyst ink onto the carbon plate electrode (1 cm^2). The working electrode was cleaned electrochemically via 50 potential cycles ranging from −0.84 to 0.30 V vs. Hg/HgO at a scan rate of 50 mV s^{-1}. The electrochemical hydrogen evolution reaction was performed at room temperature and under acidic conditions (N_2-purged KOH (1 mol/L)). The potential applied for a linear sweep voltammogram ranges from -0.58 to −2.20 V vs. a reversible hydrogen electrode with a sweep rate of 10 mV s^{-1}.

III. Result and Discussion

For preparation of H-CdS/MoS_2 HNSs, MoS_2 sheets were initially prepared through chemical exfoliation of bulk MoS_2 (Figure 2). Subsequently, the Cu precursor ($CuCl_2$) was introduced into an aqueous reaction mixture containing citric acid and sodium dodecyl sulfate (SDS). The reaction mixture was heated at 40 °C for 1 h. Following this step, an aqueous solution containing $NH_2OH{\cdot}HCl$ and NaOH was employed within the reaction mixture to facilitate the direct growth of Cu_2O cubes onto the MoS_2 sheets, resulting in the formation of Cu_2O/MoS_2 HNSs. X-ray diffraction patterns (XRD) of the obtained products exhibited characteristic peaks consistent with the cuprite structure of Cu_2O (Figure 3). Scanning electron microscopy (SEM) and transmission electron microscopy (TEM) images of the products revealed the intimate formation of cubes on MoS_2 sheets, with an average edge length of 46.60±4.28 nm (Figure 1b,e), thereby confirming the successful formation of Cu_2O/MoS_2 HNSs. High-angle annular dark-field (HAADF)-scanning TEM (STEM)-energy-dispersive X-ray spectroscopy (EDS) elemental mapping images provided further confirmation of the successful formation of the of the Cu_2O/MoS_2 HNSs (Figure 4).

Utilizing the as-prepared Cu_2O/MoS_2 HNSs, HNSs consisting of intimate contact between hollow Cu_2S cubes and MoS_2 sheets (H-Cu_2S/MoS_2 HNSs) were successfully prepared in high yield through a controlled sulfidation and acid etching process under ambient conditions. After centrifugation and dispersion of the products in methanol, an acid-etching step in 2.0 M HCl solution for approximately 30 s effectively removed the interior Cu_2O from the $Cu_2O@Cu_2S$ core-shell cubes, resulting in formation of H-Cu_2S/MoS_2 HNSs. The XRD pattern reveals the transformation of the crystal structure from Cu_2O to Cu_2S (Figure 5). The TEM images of H-Cu_2S/MoS_2 HNSs as shown in Figure 1c,f reveal an average edge length and thickness of 53.17 ± 3.51 nm. The Cu_2S hollow nanostructures of H-Cu_2S/MoS_2 HNSs retained the original cubic shape of the Cu_2O/MoS_2 HNSs[31, 32]. Furthermore, the Cu and S signals highly dispersed on hollow cubes of the products demonstrated the successful formation of H-Cu_2S/MoS_2 HNSs (Figure 1h).

The transformation of hollow Cu_2S cubes in the H-Cu_2S/MoS_2 HNSs into hollow CdS cubes during the cation exchange process leaded to the fabrication of H-CdS/MoS_2 HNSs[33-35]. TEM images reveal that hollow cubes with an average edge length of 56.96 ± 5.58 nm are formed on MoS_2 sheets (Figure 1d,g), which confirms the high-yield (>95%) production of the H-CdS/MoS_2 HNSs. The HRTEM image obtained at the interface between the hollow

CdS cube and the MoS_2 sheet reveals the formation of an intimate contact (Figure 6). This intimate contact enhances charge separation/transfer efficiency in the H-CdS/MoS_2 HNSs[36, 37]. Moreover, the CdS hollow morphology within the H-CdS/MoS_2 HNS_2 promotes enhanced light scattering, effectively increasing light harvesting efficiency[38, 39]. The XRD pattern of the H-CdS/MoS_2 HNSs displays characteristic peaks corresponding to the zincblende CdS phases (Figure 7). In addition, the HAADF-STEM-EDS elemental mapping images of the H-CdS/MoS_2 HNSs provide further confirmation of the formation of hollow CdS cubes on MoS_2 sheets (Figure 1i).

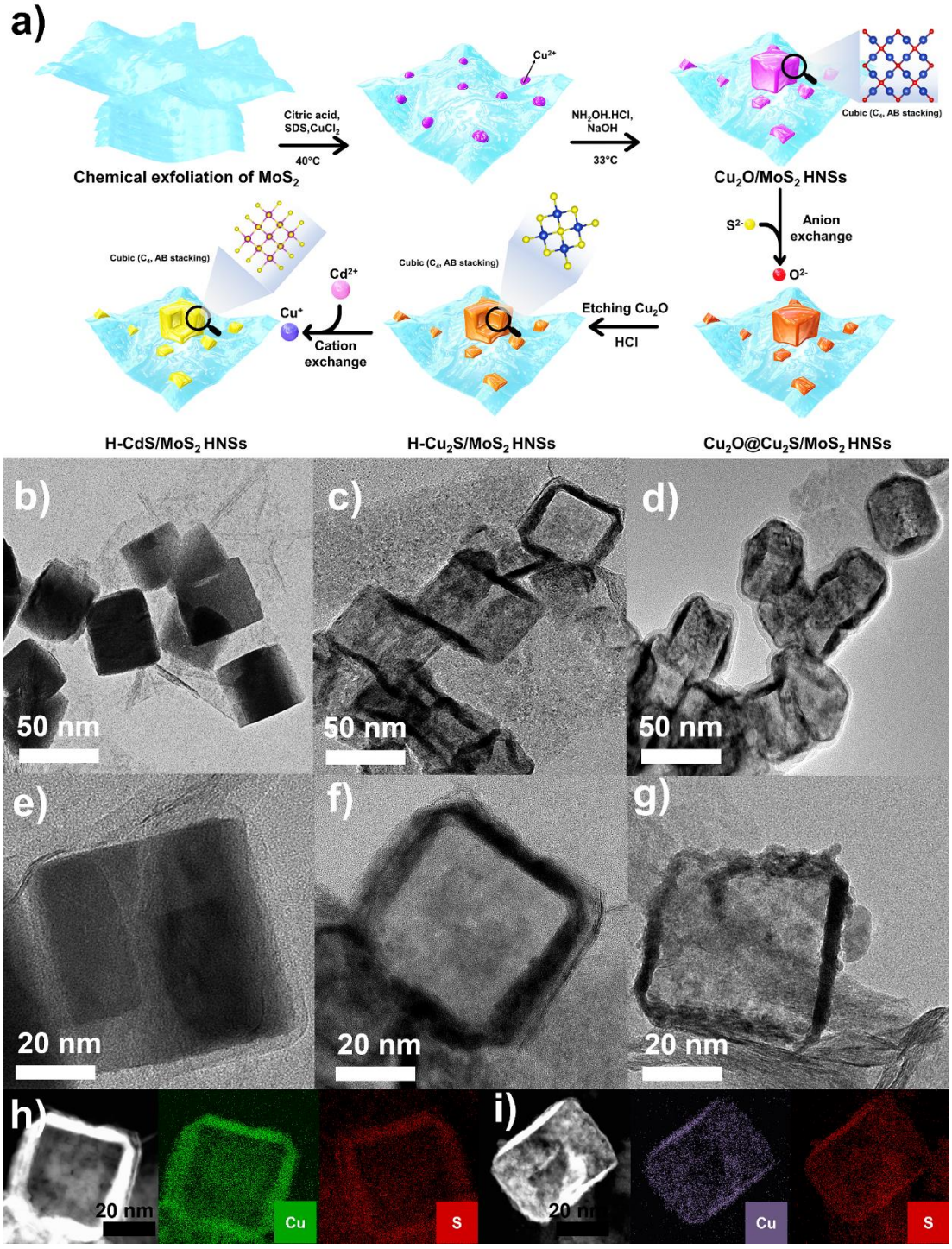

Fig.1. (a) Schematic illustration of prepared photocatalyst (b-d) low, (e-g) high magnification of TEM images. (h,i) HAADF-STEM and corresponding HAADF-STEM-EDS elemental mapping images of H-Cu_2S/MoS_2 HNSs and H-CdS/MoS_2 HNSs.

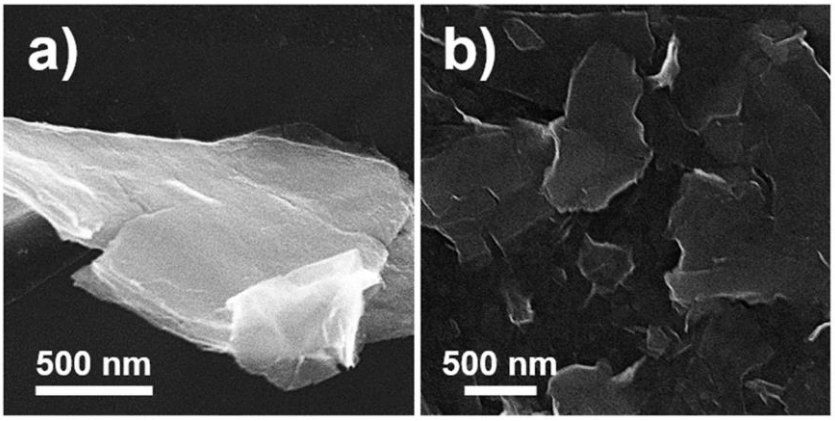

Figure 2. SEM images of (a) bulk MoS_2 and (b) MoS_2 sheets.

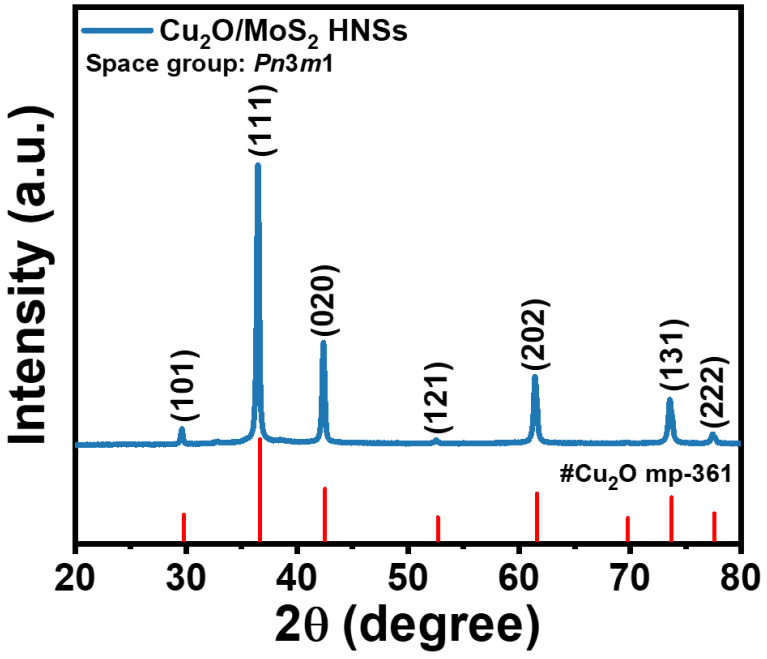

Figure 3. X-ray diffraction (XRD) patterns of Cu_2O/MoS_2 HNSs.

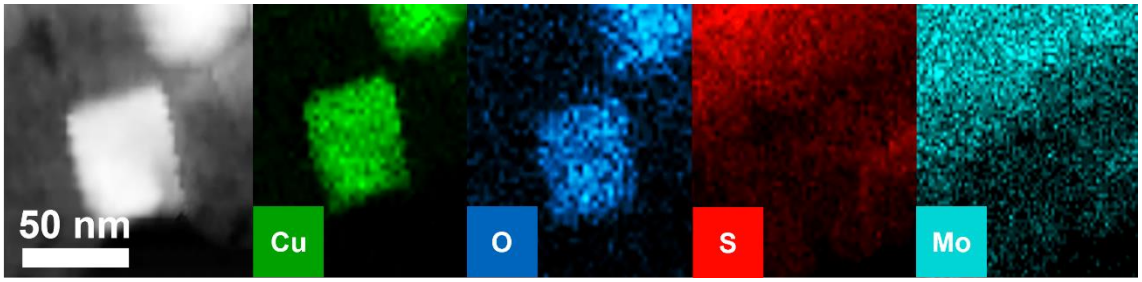

Figure 4. HAADF-STEM and corresponding HAADF-STEM-EDS elemental mapping images of Cu_2O/MoS_2 HNSs.

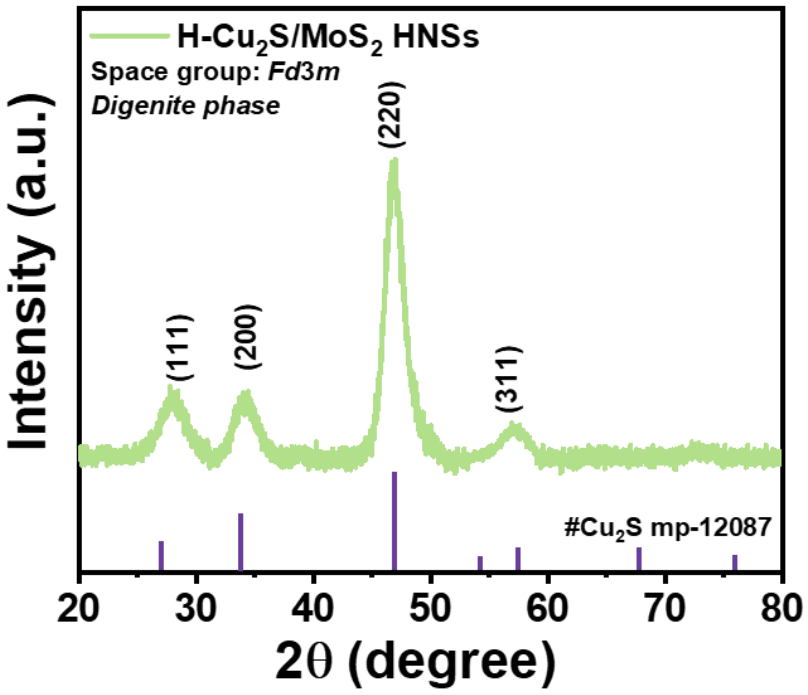

Figure 5. X-ray diffraction (XRD) patterns of H-Cu_2S/MoS_2 HNSs.

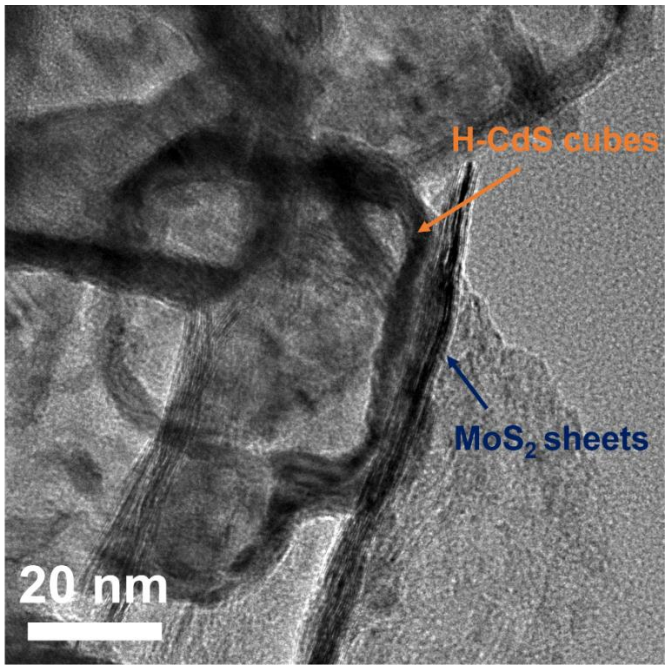

Figure 6. TEM images of H-CdS/MoS_2 HNSs.

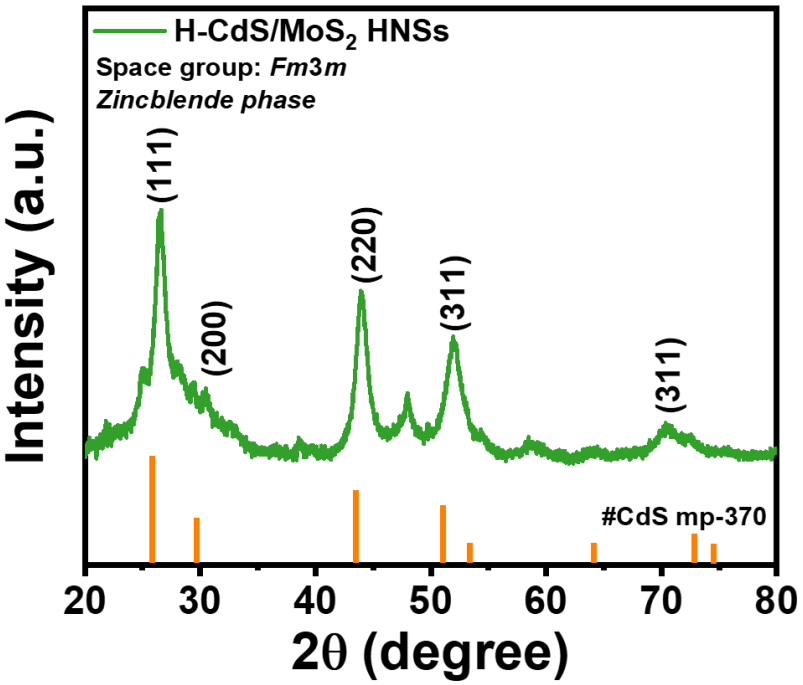

Figure 7. X-ray diffraction (XRD) patterns of H-CdS/MoS_2 H

Due to the relatively low contents and crystallinity of MoS_2 within the binary HNSs, XRD patterns of the MoS_2 component did not manifest distinguishable peaks. Consequently, XPS spectra of the Mo 3d were obtained for various HNSs to provide a more comprehensive analysis of their composition. Figure 8 depict the XPS spectra in the Mo 3d region for H-CdS/MoS_2 HNSs, H-Cu_2S/MoS_2 HNSs, and Cu_2O/MoS_2 HNSs, revealing the presence of MoS_2 sheets within the binary HNSs. Notably, all HNSs exhibited lower binding energies compared to the binding energy of Mo $3d_{5/2}$ in pristine MoS_2 sheets (Figure 9 and Table 1), indicating electron transfer from the photocatalytically active semiconductor (CdS, Cu_2S, or Cu_2O) to the MoS_2 sheets through their intimate contact. In Figure 8a, the high-resolution XPS spectrum in the Mo 3d range for H-CdS/MoS_2 HNSs exhibits a peak at approximately 225.84 eV, corresponding to the S 2s binding energy of H-CdS/MoS_2 HNSs. Similarly, the S 2s binding energy in the XPS spectra within the Mo 3d range for H-Cu_2S/MoS_2 HNSs and Cu_2O/MoS_2 HNSs was also observed (Figure 8b,c and Table 1). The double peaks observed in the Mo 3d spectrum of H-CdS/MoS_2 HNSs at 228.86 and 231.94 eV indicate the presence of the Mo^{4+} oxidation state, which was observed at more negative binding energies when compared to H-Cu_2S/MoS_2 HNSs, Cu_2O/MoS_2 HNSs, and pristine MoS_2 sheets. In the Cd 3d region, the peaks observed at 405.40 and 412.57 eV correspond to the Cd^{2+} $3d_{5/2}$ and Cd^{2+} $3d_{3/2}$ characteristic peaks originating from the H-CdS cubes within H-CdS/MoS_2 HNSs, which are higher than those of H-CdS cubes (Figure 8d and Table 2). A similar upshift in binding energies was also observed in the Cu^{2+} $3d_{3/2}$ and Cu^{2+} $3d_{1/2}$ XPS spectra of H-Cu_2S/MoS_2 HNSs and Cu_2O/MoS_2 HNSs compared to those of H-Cu_2S and Cu_2O cubes, respectively (Figure 8e,f). These shifts in binding energies of photocatalytic active semiconductors in the binary HNSs, compared to the unary cubes, can be attributed to the strong interactions between MoS_2 sheets and the photocatalytically active semiconductor. Consequently, these results collectively indicate the formation of H-CdS/MoS_2, H-Cu_2S/MoS_2, and Cu_2O/MoS_2 HNSs with intimate contact. To further investigate the incorporation of MoS_2 sheets within H-CdS/MoS_2 HNSs, we acquired the Raman spectrum of H-CdS/MoS_2 HNSs and compared it to those of pure MoS_2 sheets and H-CdS cubes (Figure 10). In the Raman spectrum of H-CdS/MoS_2 HNSs, we detected the E_{2g} and A_{1g} Raman modes at 391.54 and 421.97 cm^{-1}, respectively. These modes arise from the in-plane vibrations of MoS_2 and correspond to the peaks observed in the Raman spectrum of MoS_2 sheets. Furthermore, characteristic peaks associated with CdS were also appeared in Raman spectrum of H-CdS/MoS_2 HNSs. These findings provide evidence for the presence of both MoS_2 and CdS in the HNSs photocatalyst.

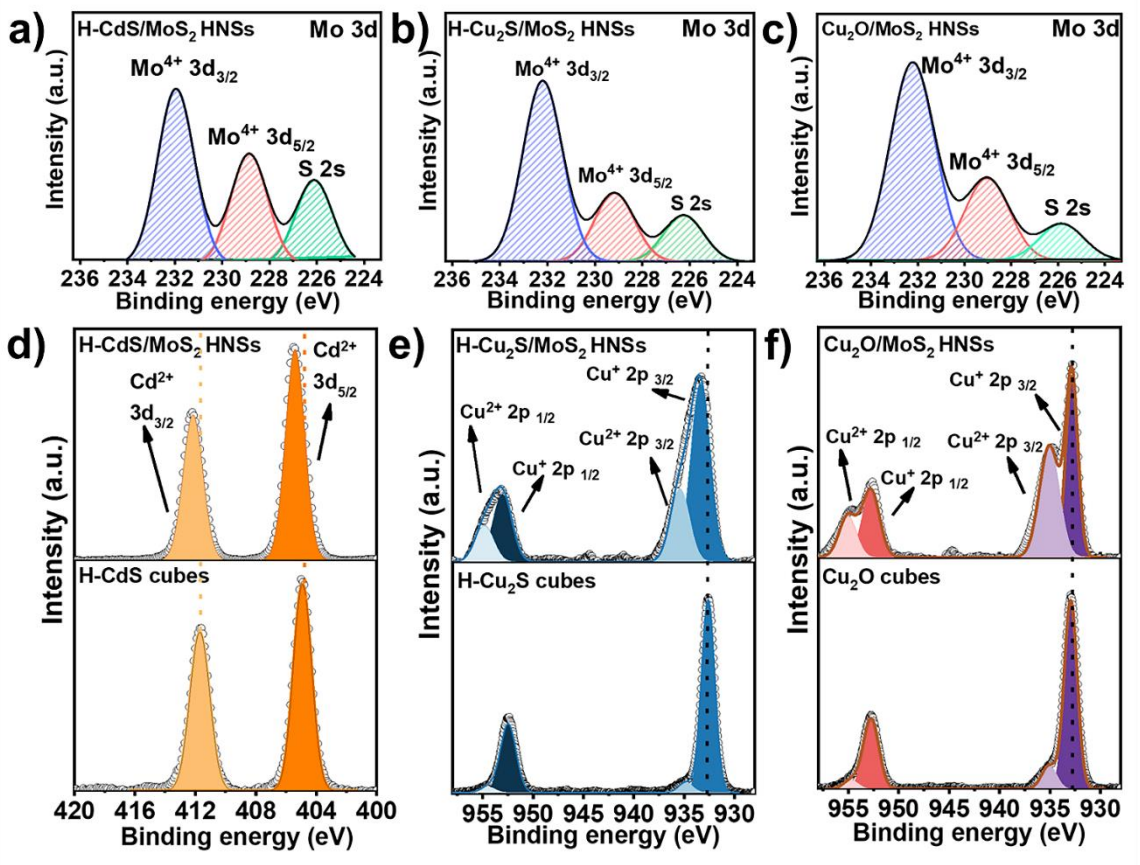

Figure 8. XPS spectra of (a-c) Mo 3d, (d) Cd 3d for H-CdS/MoS_2 HNSs, (e,f) Cu 2p for HNSs H-Cu_2S/MoS_2 HNSs and Cu_2O/MoS_2.

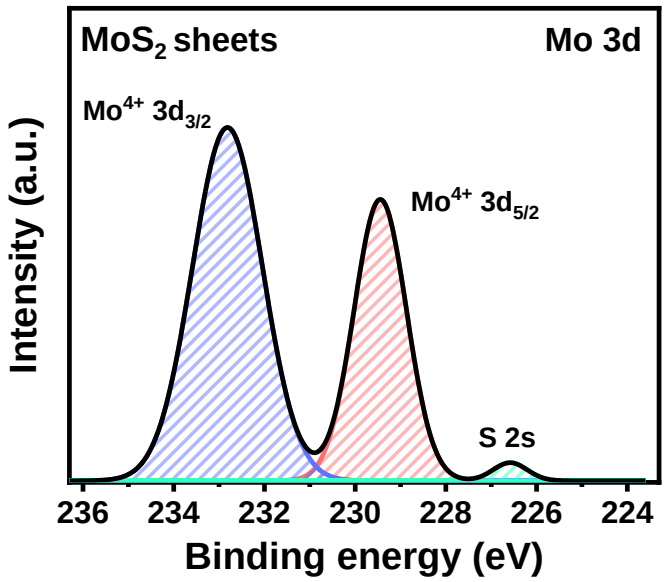

Figure 9. XPS spectra of Mo 3d for MoS_2 sheets.

Table 1. Mo 3d, S 2s, and S 2p binding energies in various catalysts.

Photocatalyst	Mo^{4+} $3d_{5/2}$	Mo^{4+} $3d_{3/2}$	S 2s	S^{2-} $2p_{3/2}$	S^{2-} $2p_{1/2}$
MoS_2 sheets	229.45 eV	232.84 eV	226.60 eV		
H-CdS/MoS_2 HNS	228.86 eV	231.94 eV	225.84 eV	161.50 eV	162.56 eV
H-Cu_2S/MoS_2 HNS	229.03 eV	232.20 eV	226.10 eV	161.73 eV	163.02 eV
Cu_2O/MoS_2 HNS	229.20 eV	232.22 eV	226.26 eV	161.92 eV	163.15 eV

Table 2. Cd 3d and Cu 2p binding energies in various catalysts.

Photocatalyst	Cd^{2+} $3d_{5/2}$	Cd^{2+} $3d_{3/2}$	Cu^{+} $2p_{3/2}$	Cu^{2+} $2p_{3/2}$	Cu^{+} $2p_{1/2}$	Cu^{2+} $2p_{1/2}$
H-CdS cubes	404.91 eV	411.70 eV				
H-CdS/MoS_2 HNS	405.40 eV	412.57 eV				
Cu_2O cubes			932.94 eV	935.07 eV	952.76 eV	954.76 eV
Cu_2O/MoS_2 HNS			932.83 eV	935.05 eV	952.78 eV	955.06 eV
H-Cu_2S cubes			932.62 eV	934.83 eV	952.47 eV	954.47 eV
H-Cu_2S/MoS_2 HNS			933.41 eV	935.42 eV	953.04 eV	954.82 eV

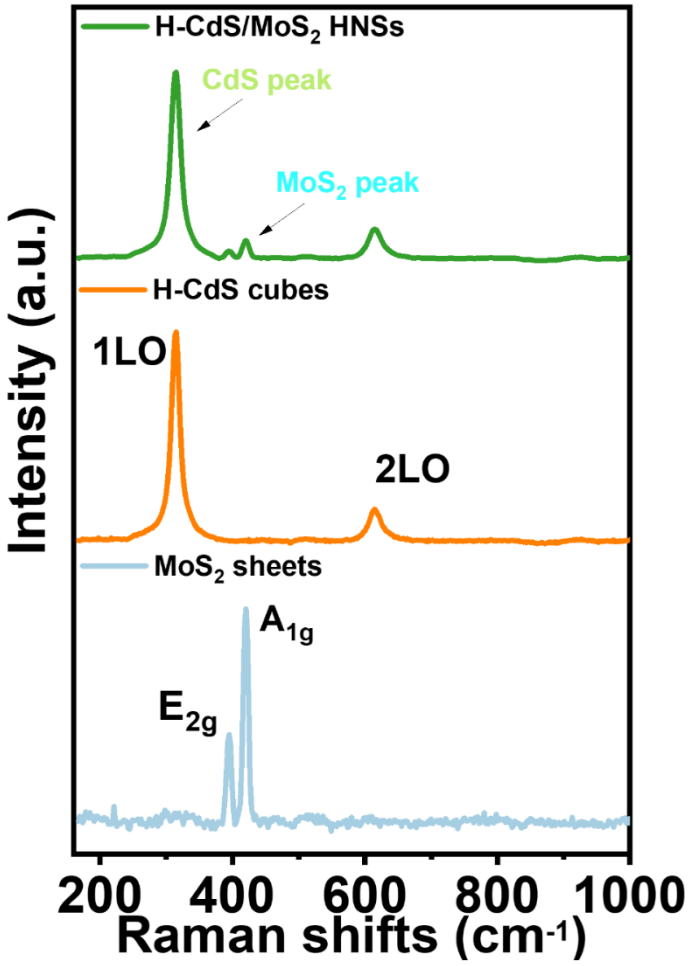

Figure 10. Raman spectra of H-CdS/MoS_2 HNSs, H-CdS cubes, and MoS_2 sheets

To explore the impact of the intimate interface and the hollow CdS structure within H-CdS/MoS_2 HNSs on photocatalysis, we examined the photocatalytic hydrogen evolution activity of the H-CdS/MoS_2 HNSs in water including methanol as a hole scavenger under visible light irradiation ($\lambda > 420$ nm). The photocatalytic performance of H-CdS/MoS_2 HNSs for hydrogen evolution was compared with that of H-Cu_2S/MoS_2 HNSs, Cu_2O/MoS_2 HNSs, and their respective unary counterparts, including H-CdS cubes, H-Cu_2S cubes, Cu_2O cubes, and MoS_2 sheets (Figure 11). Figure 12a,b display the hydrogen evolution for both binary and unary photocatalysts. MoS_2 sheets exhibited negligible photocatalytic hydrogen evolution activity due to their low light harvesting[40, 41]. On the other hand, all binary HNSs containing MoS_2 sheets manifested significantly higher hydrogen evolution rates compared to their unary photocatalyst counterparts such as H-CdS, H-Cu_2S, and Cu_2O cubes, respectively. These findings demonstrate the pivotal role of forming intimate interfaces between photocatalytically active semiconductor and MoS_2 sheets in promoting the rate of the photocatalytic hydrogen evolution reaction. Among various photocatalysts, H-CdS/MoS_2 HNSs exhibited the highest rate of photocatalytic hydrogen evolution at 440.3 μmol g^{-1} h^{-1}, surpassing Cu_2O cubes (41.0 μmol g^{-1} h^{-1}), hollow Cu_2S cubes (50.4 μmol g^{-1} h^{-1}), hollow CdS cubes (78.6 μmol g^{-1} h^{-1}), Cu_2O/MoS_2 HNSs (196.0 μmol g^{-1} h^{-1}), and H-Cu_2S/MoS_2 HNSs (345.4 μmol g^{-1} h^{-1}) by 10.7, 8.7, 5.6, 2.2, and 1.3 times, respectively (Figure 12b). Notably, when comparing the photocatalytic hydrogen evolution activity between binary HNSs and their unary counterparts (H-CdS/MoS_2 HNSs vs. H-CdS cubes, H-Cu_2S/MoS_2 HNSs vs. H-Cu_2S cubes, and Cu_2O/MoS_2 HNSs vs. Cu_2O cubes), the photocatalytic activity of Cu_2O/MoS_2 HNSs was 4.8 fold higher compared to Cu_2O cubes, which can be attributed solely to the promoting effects resulting from the formation of intimate interface between Cu_2O cubes and MoS_2 sheets. On the other hand, H-CdS/MoS_2 and H-Cu_2S/MoS_2 HNSs exhibited 5.6 and 6.9 fold increases in photocatalytic hydrogen evolution activity compared to their respective unary photocatalysts. These findings demonstrated that the combination of the hollow structure of the photocatalytically active semiconductor and MoS_2 sheets more effectively enhances the photocatalytic hydrogen evolution reaction. To further explore the photocatalytic activity of the HNSs, cyproflaxin degradation experiments with various photocatalysts were performed under dark and visible-light irradiation ($\lambda > 420$ nm). In the dark, all photocatalysts showed negligible photocatalytic degradation (Figure 12c). Figure 12d,e show the normalized concentration changes in cyproflaxin (C/C_0) and variation of $\ln(C/C_0)$ versus the reaction time for the different photocatalysts, respectively. The photocatalytic cyproflaxin degradation trend in the presented catalysts was similar to that in

the hydrogen evolution activity (Figure 12f). In addition, photocatalytic activity for methyl orange degradation also exhibited analogous results with those of hydrogen evolution reaction and cyproflaxin degradation (Figure 13). The results of the photocatalysis experiments unambiguously confirm that the combined morphological and compositional advantages of H-CdS/MoS_2 HNSs effectively enhance the photocatalytic performances[42, 43].

The photocatalytic stability of H-CdS/MoS_2 HNSs was investigated by estimating hydrogen evolution over an irradiation time of 30 h. H-CdS/MoS_2 HNSs retained significantly higher photocatalytic activity compared to H-CdS cubes throughout the 30 h duration, thereby demonstrating the superior stability of H-CdS/MoS_2 HNSs for photocatalytic hydrogen evolution reaction (Figure 12g). Furthermore, we assessed the hydrogen evolution rate of H-CdS/MoS_2 HNSs through four consecutive cycles of repeated hydrogen evolution reactions under standard conditions to further confirm their exceptional stability. The hydrogen evolution activity of H-CdS/MoS_2 HNSs remained nearly constant over the four repeated cycles, with the hydrogen evolution activity measured after the fourth cycle at 91.5% compared to that observed during the first cycle (Figure 12h). In stark contrast, the hydrogen evolution activity of H-CdS cubes after four cycles was only about 14.1% of the initial activity observed after the first cycle (Figure 12i). These results further demonstrate the critical role played by the combination of H-CdS cubes and MoS_2 sheets in enhancing photocatalytic stability.

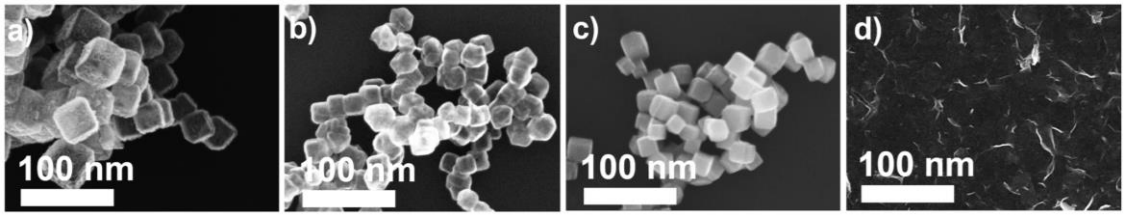

Figure 11. SEM images of pristine photocatalyst (a) H-CdS cubes, (b) H-Cu_2S cubes, and (c) Cu_2O cubes and (d) MoS_2 sheets

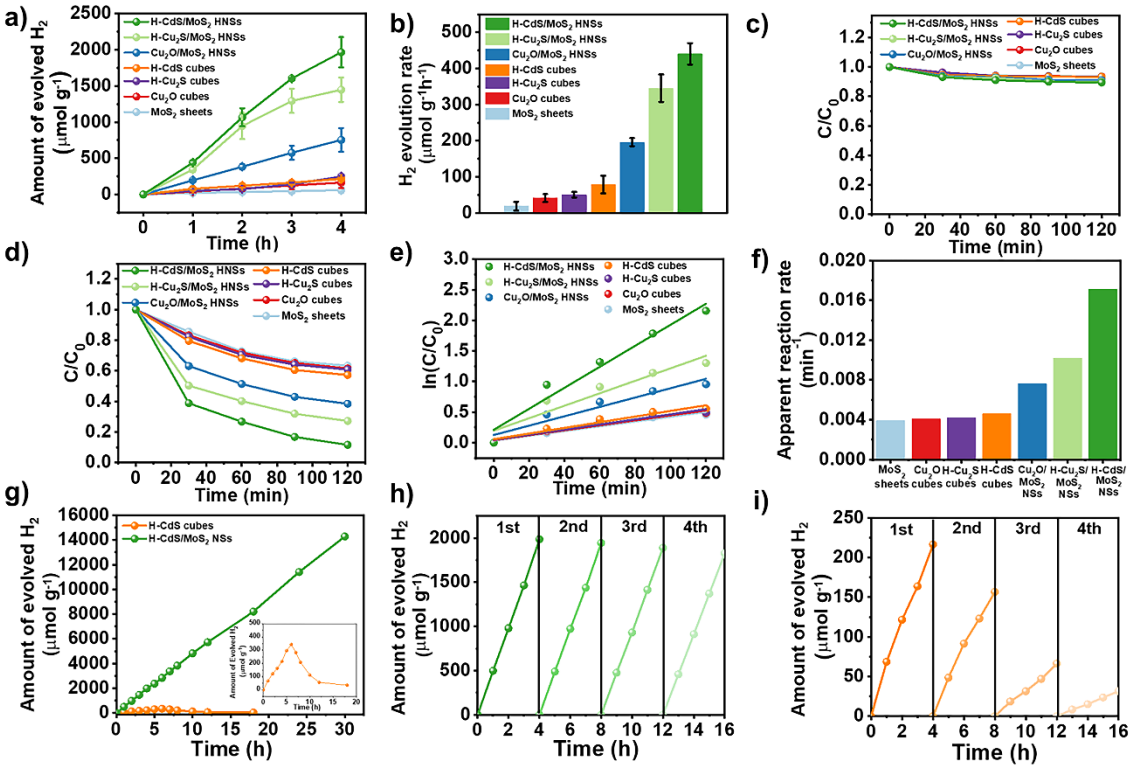

Figure 12. (a) Amounts of hydrogen evolved during the photocatalysis and (b) corresponding hydrogen evolution rates obtained with various catalysts under visible light irradiation ($\lambda > 420$ nm). Photodegradation of Ciprofloxacin vs time using different photocatalysts under (c) dark and (d) visible light irradiation ($\lambda > 420$ nm). (e) Variation of $\ln(C/C_0)$ vs visible light irradiation and (f) corresponding apparent reaction rate. (g) Long-term stability test of H-CdS cubes and H-CdS/MoS_2 HNSs. (h,i) Cycling test of photocatalytic activity by H-CdS cubes and H-CdS/MoS_2 HNSs over 16 h.

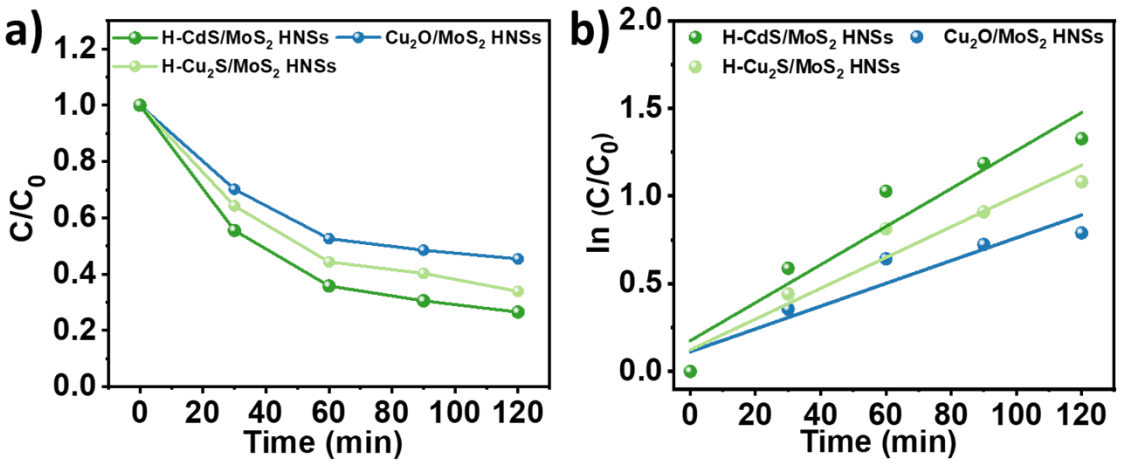

Figure 13. MO degradation over the prepared catalysts.

To gain insight into the behavior of photo-induced charge carriers in H-CdS/MoS_2 HNSs, we established the band structure using the conduction band (CB) edge potentials and band gaps of the H-CdS cubes and MoS_2 sheets. The band gap of the H-CdS cubes (Eg = 2.38 eV) and MoS_2 sheets (Eg = 1.80 eV) was determined using Tauc plots derived from the Kubelka-Munk function, respectively (Figure 14a,b). To investigate the CB edge potential of both the H-CdS cubes and MoS_2 sheets, we obtained Mott-Schottky curves at different frequencies. In the Mott-Schottky curves, the positive slopes reveal the n-type semiconductor properties of both the H-CdS cubes and MoS_2 sheets (Figure 14c,d). For n-type semiconductors, it is well-established that the flat band potential measured according to the Mott–Schottky method is close to the CB of the semiconductor[44]. Based on their Mott-Schottky curves obtained at different frequencies, we determined the flat band potentials of the H-CdS cubes and MoS_2 sheets to be -0.45 and -0.30 V, respectively. Utilizing the band gaps and flat band potentials of the H-CdS cubes and MoS_2 sheets, we constructed the band structure of H-CdS/MoS_2 HNSs (Figure 14e). With the band structure of H-CdS/MoS_2 HNSs, it can be anticipated that photo-induced electrons in the CB of the hollow CdS cubes, possessing a more negative potential, spontaneously migrate to the CB of MoS_2 sheets under irradiation. This migration of electrons from the hollow CdS cubes to the MoS_2 sheets in the H-CdS/MoS_2 HNSs promotes the hydrogen evolution reaction.

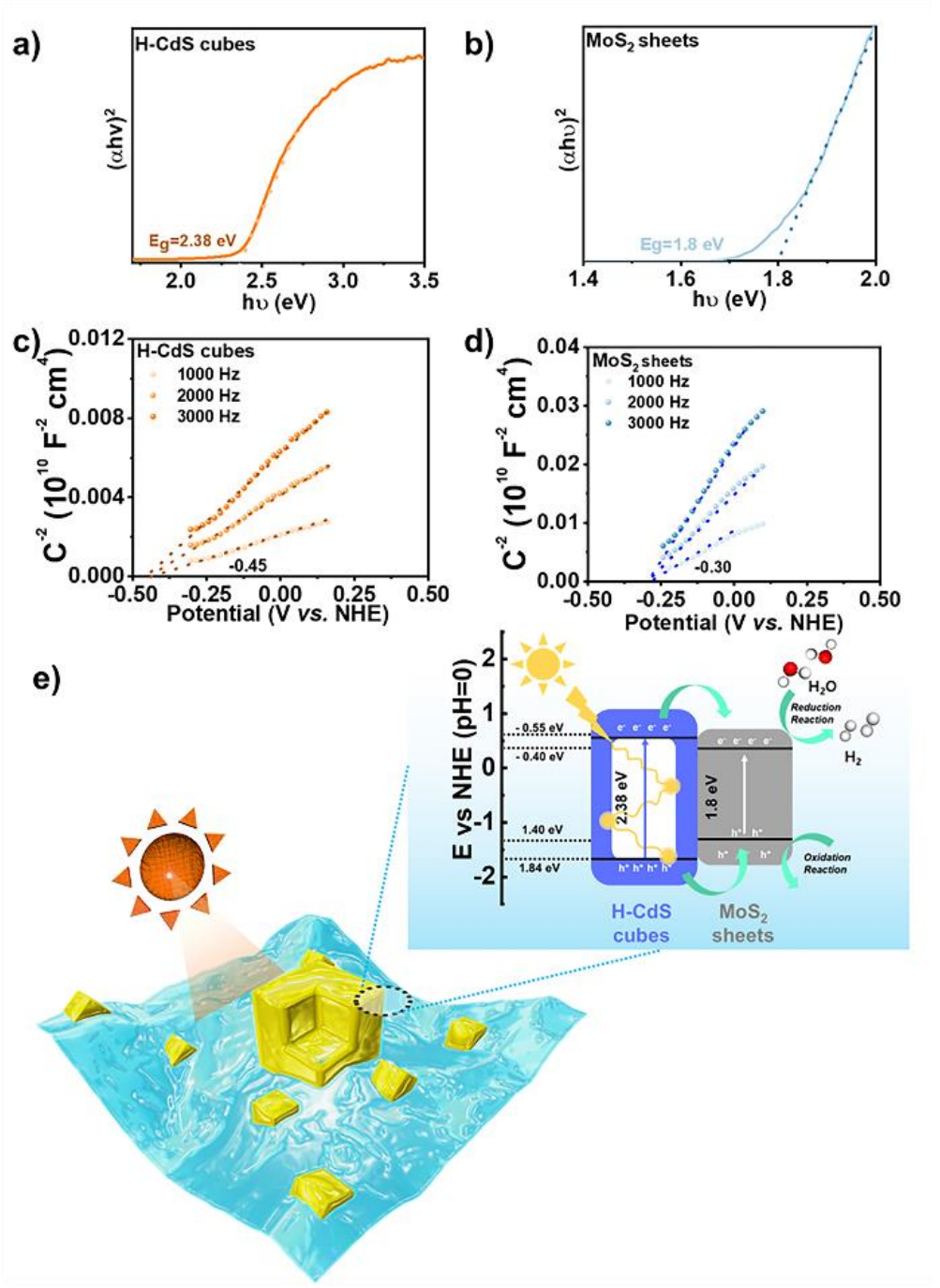

Figure 14. Tauc plots, Mott-Schottky plots of (a,c) H-CdS cubes and (b,d) MoS_2 sheets. (e) Band structures and proposed photocatalytic mechanism of H-CdS/MoS_2 NSs under visible light irradiation ($\lambda > 420$ nm).

It is widely accepted that photocatalytic performance is highly dependent on charge separation/transfer efficiency, capability to retard charge recombination, light harvesting efficiency, and co-catalytic activity of the photocatalysts[36, 45, 46]. EIS plots for the binary HNSs were acquired to verify the effective separation and transfer of photo-induced charges in H-CdS/MoS_2 HNSs, as EIS measurements serve as a valuable tool for investigating charge transfer at the interface between the semiconductor and electrolyte[47]. In Figure 15, the Nyquist plot of MoS_2 sheets reveals a smaller radius compared to H-CdS, H-Cu_2S, and Cu_2O cubes, signifying the superior charge separation and transfer efficiency of MoS_2 sheets over unary cubes. Due to this property of MoS_2 sheets, all binary HNSs exhibited enhanced charge separation/transfer efficiency compared to their unary cube counterparts, respectively. Remarkably, the Nyquist plot of H-CdS/MoS_2 HNSs exhibits a significantly smaller radius compared to H-Cu_2S/MoS_2 and Cu_2O/MoS_2 HNSs. This observation highlights the exceptional charge separation and transfer efficiency of H-CdS/MoS_2 HNSs relative to different photocatalyst, which can contribute to the higher hydrogen evolution activity of H-CdS/MoS_2 HNSs. In addition, to further elucidate the catalytic activity for hydrogen evolution of the photocatalysts, we measured the electrocatalytic activities of various photocatalysts for hydrogen evolution reaction in N_2-saturated alkaline media in the dark and visible-light irradiation (Figure 15b,c). In the dark, trend of the electrochemical hydrogen evolution reaction activity was identical to that of photocatalytic hydrogen evolution reaction activity, which indicate that combination of H-CdS cubes and MoS_2 sheets is more effective to promote hydrogen evolution compared to other combinations such as H-Cu_2S/MoS_2 and Cu_2O/MoS_2 HNSs. These findings signify the superior co-catalytic activity of H-CdS/MoS_2 HNSs than different binary and unary photocatalysts for hydrogen evolution reaction. Interestingly, under visible light irradiation (λ > 420 nm), the extent of enhancement in hydrogen evolution reaction activity exhibited by the H-CdS/MoS_2 HNSs, when compared to their activity measured in the dark, was significantly greater than that observed for other catalysts. Based on 30 mA cm^{-2}, overpotential of H-CdS/MoS_2 HNSs was decreased as 397.03 mV, whereas 482.5, 567.89, and 737.5 mV of overpotential was reduced for Cu_2S/MoS_2 HNSs, Cu_2O/MoS_2 HNSs, and hollow CdS cubes, respectively. These results clearly demonstrate that higher photocatalytic hydrogen evolution reaction activity of H-CdS/MoS_2 HNSs than other photocatalysts is attributed to not only cocatalytic activity for hydrogen evolution reaction but also higher light harvesting ability. Taken together, the higher charge transfer capability, co-catalytic activity, and light harvesting ability of H-CdS/MoS_2 HNSs than other photocatalysts can result in more enhanced photocatalytic

performance of the H-CdS/MoS_2 HNSs.

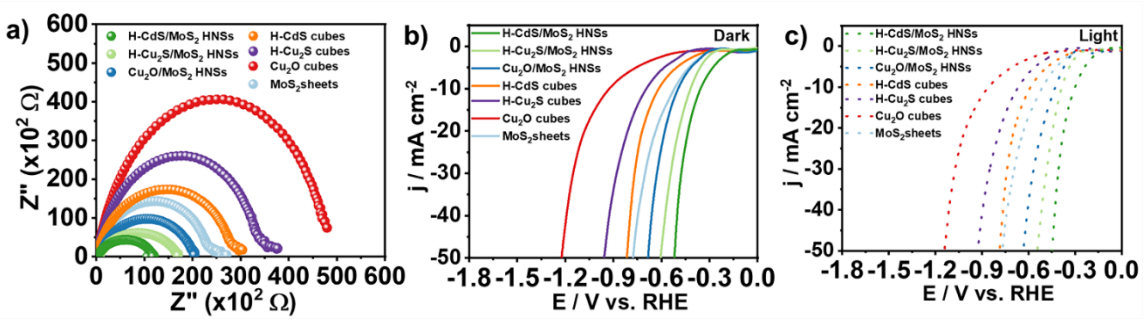

Figure 15. (a) EIS spectra of various photocatalyst. Polarization curves of various photocatalyst in (b) dark and at (c) visible-light irradiation.

IV. Conclusion

In summary, we have successfully synthesized H-CdS/MoS_2 HNSs through a sequential process involving the direct growth of Cu_2O cubes on MoS_2 sheets, anion and cation exchange methods. This approach allows for the preparation of hollow CdS cubes and intimate interfaces between these hollow CdS cubes and MoS_2 sheets. The resulting H-CdS/MoS_2 HNSs demonstrate superior photocatalytic performance in hydrogen evolution and pollutant degradation when compared to their binary and unary counterparts. The hollow CdS morphology offers increased active sites and enhanced light absorption capability due to multi-scattering within their interior. Furthermore, the intimate interface between hollow CdS cubes and MoS_2 sheets enhances charge separation and transfer capabilities as well as co-catalytic activity. These exceptional outcomes are attributed to the combination of intimate interfaces and the morphology of hollow CdS cubes, which collectively enhance charge transfer, intrinsic hydrogen evolution activity, and light absorption. This innovative approach has the potential for broad applications and opens up opportunities to enhance charge transfer, intrinsic catalytic activity, and light absorption in various photocatalytic processes.

V. References

[1]. Shen R, Li X, Qin C, Zhang P, Li X. Efficient photocatalytic hydrogen evolution by modulating excitonic effects in Ni-intercalated covalent organic frameworks. Adv Energy Mater. 2023;13(13):2203695.

[2]. Huang W, Su C, Zhu C, Bo T, Zuo S, Zhou W, et al. Isolated electron trap-induced charge accumulation for efficient photocatalytic hydrogen production. Angew Chem Int Ed 2023;62(25):e202304634.

[3]. Liu J, Wu M, Ye H, Xie Y, Ma Y, Liu L. Strong interaction between sulfur sites and oxygen vacancies in Z-Scheme $ZnIn_2S_4/TiO_{2-x}$ heterojunction for improved photocatalytic hydrogen yield and stability. Chem Eng J. 2023;455:140722.

[4]. Somoye OA. Energy crisis and renewable energy potentials in Nigeria: A review. Renew Sust Energ Rev. 2023;188:113794.

[5]. Muthukumar K, Leban L, Sekar A, Elangovan A, Sarkar N, Li J. Tuning the defects in MoS_2/reduced graphene oxide 2D hybrid materials for optimizing battery performance. Sustain Energ Fuels. 2021;5(16):4002-14.

[6]. Thangamuthu M, Vankayala K, Xiong L, Conroy S, Zhang X, Tang J. Tungsten oxide-based Z-Scheme for visible light-driven hydrogen production from water splitting. ACS Catal. 2023;13(13):9113-24.

[7]. Li X, Raorane CJ, Xia C, Wu Y, Tran TKN, Khademi T. Latest approaches on green hydrogen as a potential source of renewable energy towards sustainable energy: Spotlighting of recent innovations, challenges, and future insights. Fuel. 2023;334.

[8]. Nagella SR, Vijitha R, Ramesh Naidu B, Krishna Rao KSV, Ha C-S, Venkateswarlu K. Benchmarking recent advances in hydrogen production using g-C_3N_4-based photocatalysts. Nano Energy. 2023;111.

[9]. Shen J, Luo C, Qiao S, Chen Y, Tang Y, Xu J, et al. Single-atom Cu channel and N-vacancy engineering enables efficient charge separation and transfer between C_3N_4 interlayers for boosting photocatalytic hydrogen production. ACS Catal. 2023;13(9):6280-8.

[10]. Li Y, Li H, Li S, Li M, He P, Xiao Y, et al. Boosting the photocatalytic hydrogen evolution performance by fabricating the NiO/Zn3In2S6 p-n heterojunction. Appl Surf Sci. 2024;642:158622.

[11]. Wu C, Huang W, Liu H, Lv K, Li Q. Insight into synergistic effect of Ti_3C_2 M-Xene and MoS_2 on anti-photocorrosion and photocatalytic of CdS for hydrogen production. Appl Catal

B-Environ. 2023;330:122653.
[12]. Lei Y, Ng KH, Zhu Y, Zhang Y, Li Z, Xu S, et al. Mo-activated VC as effective cocatalyst for an enhanced photocatalytic hydrogen evolution activity of CdS. Chem Eng J. 2023;452:139325.
[13]. Wang X, Wu K, Cao W, Rui K, Wang W, Zhu R, et al. Z-Scheme strategy in polymeric graphitic C_3N_5/CdS core–shell heterojunction drives long-lived carriers separation for robust visible-light hydrogen production. Adv Mater Interfaces. 2022;10(5):2201627.
[14]. Yu E-J, Kim HC, Kim HJ, Jung S-Y, Ryu K-S, Choi S-I, et al. Anisotropic heteronanocrystals of Cu_2O–2D MoS_2 for efficient visible light driven photocatalysis. Appl Surf Sci. 2021;538:148159.
[15]. Li W, Liu C, Gu C, Choi JH, Wang S, Jiang J. Interlayer Charge Transfer Regulates Single-Atom Catalytic Activity on Electride/Graphene 2D Heterojunctions. J Am Chem Soc. 2023;145(8):4774-83.
[16]. Azizar GAB, Hong JW. Optimizing intrinsic cocatalyst activity and light absorption efficiency for efficient hydrogen evolution of 1D/2D ReS_2-CdS photocatalysts via control of ReS_2 nanosheet layer growth. J Mater Sci Technol. 2024;168:103-13.
[17]. Bang J, Das S, Yu EJ, Kim K, Lim H, Kim S, et al. Controlled photoinduced electron transfer from InP/ZnS quantum dots through Cu doping: a new prototype for the visible-light photocatalytic hydrogen evolution reaction. Nano Lett. 2020;20(9):6263-71.
[18]. Dolai S, Maiti P, Ghorai A, Bhunia R, Paul PK, Ghosh D. Exfoliated molybdenum disulfide-wrapped CdS nanoparticles as a nano-heterojunction for photo-electrochemical water splitting. ACS Appl Mater Interfaces. 2021;13(1):438-48.
[19]. Wi DH, Park SY, Lee S, Sung J, Hong JW, Han SW. Metal–semiconductor ternary hybrids for efficient visible-light photocatalytic hydrogen evolution. J Mater Chem A. 2018;6(27):13225-35.
[20]. Han B, Liu S, Zhang N, Xu Y-J, Tang Z-R. One-dimensional CdS@MoS_2 core-shell nanowires for boosted photocatalytic hydrogen evolution under visible light. Appl Catal B-Environ. 2017;202:298-304.
[21]. Mafa PJ, Malefane ME, Opoku F, Mamba BB, Kuvarega AT. Visible light responsive MoS_2/Ag@WO_3/EG photoanode with highly stable Z-scheme induced circular electron motion pioneered by exfoliated graphite for bisphenol a photoelectrodegradation. Chem Eng J. 2023;464:142462.
[22]. Liu X, Chen J, Hu Y, Pan Q, Zhong H, Zeng R, et al. Optimization of the in-plane activity of MoS_2 monolayer by Pd-S bonds for hydrogen evolution reaction. Appl Surf Sci.

2024;642:158563.
[23]. Ruqia B, Kanti Kabiraz M, Wook Hong J, Choi S-I. Catalyst activation: Surface doping effects of group VI transition metal dichalcogenides towards hydrogen evolution reaction in acidic media. J Energy Chem. 2022;72:217-40.
[24]. Sun W, Pang H, Khan SU, Yang R, Wu Q, Ma H, et al. Highly Efficient Photocatalysts: Polyoxometalate Synthons Enable Tailored CdS-MoS_2 Morphologies and Enhanced H(2) Evolution. ACS Appl Mater Interfaces. 2023;15(29):35611-21.
[25]. Dai B, Guo J, Gao C, Yin H, Xie Y, Lin Z. Recent advances in efficient photocatalysis via modulation of electric and magnetic fields and reactive phase control. Adv Mater. 2023;35(14):e2210914.
[26]. Zhang L, Jiang X, Jin Z, Tsubaki N. Spatially separated catalytic sites supplied with the CdS–MoS_2–In_2O_3 ternary dumbbell S-scheme heterojunction for enhanced photocatalytic hydrogen production. J Mater Chem A. 2022;10(19):10715-28.
[27]. Fu Y, Fan B, Chang S, Guo D, Wang F, Pan Q. An ultrasensitive photoelectrochemical assay for tumor necrosis factor-alpha based on hollow CdS cubes as a signal generator and $NiCo_2O_4$-Au as a signal extinguisher. Analyst. 2023;148(19):4746-52.
[28]. Wu C, Wu K, Bai W, Li N, Gao Y, Ge L. CoPx co-catalyst decorated CdS hollow nanocubes as efficient photocatalysts for hydrogen production under visible light irradiation. Colloid Surf A-Physicochem Eng Asp. 2023;666:131368.
[29]. Cui S, Ao R, Lin Z, Ding M. Phosphorous-doped cadmium sulfide hollow octahedrons for enhanced visible-light photocatalytic H_2 evolution. Int J Hydrog Energy. 2023.
[30]. Hong JW. Highly active binary exfoliated MoS_2 sheet–Cu_2O nanocrystal hybrids for efficient photocatalytic pollutant degradation. Bull Korean Chem Soc. 2020;41(12):1147-52.
[31]. Cao W, Guo T, Wang J, Xu G, Jiang J, Liu D. Cu-based materials: Design strategies (hollow, core-shell, and LDH), sensing performance optimization, and applications in small molecule detection. Coord Chem Rev. 2023;497:215450.
[32]. Lee Y-I. Selective transformation of Cu nanowires to Cu_2S or CuS nanostructures and the roles of the Kirkendall effect and anion exchange reaction. Mater Chem Phys. 2016;180:104-13.
[33]. Toe CY, Zheng Z, Wu H, Scott J, Amal R, Ng YH. Transformation of cuprous oxide into hollow copper sulfide cubes for photocatalytic hydrogen generation. J Phys Chem C. 2018;122(25):14072-81.
[34]. Hsin-Lun W RS, Atsushi Y, Masato K, Mitsutaka H, Hiroki K TT. Formation of pseudomorphic nanocages from Cu_2O nanocrystals through anion exchange reactions.

Science. 2016;351(6279):1306.
[35]. Zhang Y, Ran L, Li Z, Zhai P, Zhang B, Fan Z, et al. Simultaneously efficient solar light harvesting and charge transfer of hollow octahedral Cu_2S/CdS p–n heterostructures for remarkable photocatalytic hydrogen generation. Transactions Tianjin Univ. 2021;27(4):348-57.
[36]. Moon HS, Hsiao KC, Wu MC, Yun Y, Hsu YJ, Yong K. Spatial separation of cocatalysts on Z-Scheme organic/inorganic heterostructure hollow spheres for enhanced photocatalytic H_2 evolution and in-depth analysis of the charge-transfer mechanism. Adv Mater. 2023;35(4):e2200172.
[37]. Feng X, Shang H, Zhou J, Ma X, Gao X, Wang D, et al. Heterostructured core–shell $CoS_{1.097}$@$ZnIn_2S_4$ nanosheets for enhanced photocatalytic hydrogen evolution under visible light. Chem Eng J. 2023;457:141192.
[38]. Zhang C, Liang Q, Wang Y, Zhou M, Li X, Xu S, et al. Construction of Z-scheme heterojunction CoS/CdS@g-C_3N_4 hollow sphere with spatical charge separation for enhanced photocatalytic hydrogen production. Appl Surf Sci. 2023;626:157214.
[39]. Zhang S, Du S, Wang Y, Han Z, Li X, Li G, et al. Synergy of yolk-shelled structure and tunable oxygen defect over CdS/$CdCO_3$-CoS_2: Wide band-gap semiconductors assist in efficient visible-light-driven H_2 production and CO_2 reduction. Chem Eng J. 2023;454:140113.
[40]. Yin XL, Li LL, Jiang WJ, Zhang Y, Zhang X, Wan LJ, et al. MoS_2/CdS nanosheets-on-nanorod heterostructure for highly efficient photocatalytic H_2 generation under visible light irradiation. ACS Appl Mater Interfaces. 2016;8(24):15258-66.
[41]. Lin H, Li Y, Li H, Wang X. Multi-node CdS hetero-nanowires grown with defect-rich oxygen-doped MoS2 ultrathin nanosheets for efficient visible-light photocatalytic H_2 evolution. Nano Res. 2017;10(4):1377-92.
[42]. Yu X, Du R, Li B, Zhang Y, Liu H, Qu J, et al. Biomolecule-assisted self-assembly of CdS/MoS_2/graphene hollow spheres as high-efficiency photocatalysts for hydrogen evolution without noble metals. Appl Catal B-Environ. 2016;182:504-12.
[43]. Liu T, Shen H, Wang M, Feng Q, Chen L, Wang W, et al. Fabrication of ZnIn2S4 nanosheets decorated hollow CdS nanostructure for efficient photocatalytic H2-evolution and antibiotic removal performance. Sep Purif Technol. 2023;315:123698.
[44]. Mai S-S, Hsiao K-Y, Yang Y-C, Lu Y-R, Lu M-Y, Hsieh Y-Y, et al. Synchronous regulation of Schottky/p-n dual junction in Prussian blue-derived Janus heterostructures: A path to ultrafast long life potassium ion batteries. Chem Eng J. 2023;474:145992.

[45]. Yuan Z, Cao Y, Meng Y, Pan G, Zheng Y, Ni Z, et al. The construction of lattice-matched CdS-Ag(2)S heterojunction photocatalysts: High-intensity built-in electric field effectively boosts bulk-charge separation efficiency. J Hazard Mater. 2023;458:131895.
[46]. Gao W, Zhao X, Zhang T, Yu X, Ma Y, dos Santos EC, et al. Construction of diluted magnetic semiconductor to endow nonmagnetic semiconductor with spin-regulated photocatalytic performance. Nano Energy. 2023;110:108381.
[47]. Chong W-K, Ng B-J, Kong XY, Tan L-L, Putri LK, Chai S-P. Non-metal doping induced dual p-n charge properties in a single $ZnIn_2S_4$ crystal structure provoking charge transfer behaviors and boosting photocatalytic hydrogen generation. Appl Catal B-Environ. 2023;325:122372.